Three-Dimensional Cellular Deformation Analysis with a Two-Photon Magnetic Manipulator Workstation

Hayden Huang,* Chen Y. Dong,* Hyuk-Sang Kwon,* Jason D. Sutin,† Roger D. Kamm,* and Peter T. C. So*
*Department of Mechanical Engineering, MIT, Cambridge, Massachusetts 02139; and †University of Illinois, Urbana-Champaign, Illinois 61801 USA

ABSTRACT The ability to apply quantifiable mechanical stresses at the microscopic scale is critical for studying cellular responses to mechanical forces. This necessitates the use of force transducers that can apply precisely controlled forces to cells while monitoring the responses noninvasively. This paper describes the development of a micromanipulation workstation integrating two-photon, three-dimensional imaging with a high-force, uniform-gradient magnetic manipulator. The uniform-gradient magnetic field applies nearly uniform forces to a large cell population, permitting statistical quantification of select molecular responses to mechanical stresses. The magnetic transducer design is capable of exerting over 200 pN of force on 4.5-μm-diameter paramagnetic particles and over 800 pN on 5.0-μm ferromagnetic particles. These forces vary within $\pm$10% over an area 500 $\times$ 500 μm^2. The compatibility with the use of high numerical aperture ($\approx$1.0) objectives is an integral part of the workstation design allowing submicron-resolution, three-dimensional, two-photon imaging. Three-dimensional analyses of cellular deformation under localized mechanical strain are reported. These measurements indicate that the response of cells to large focal stresses may contain three-dimensional global deformations and show the suitability of this workstation to further studying cellular response to mechanical stresses.

INTRODUCTION

How cells respond to mechanical stresses is relevant in many physiological systems, including bone remodeling and cardiovascular disease (Burger and Klein-Nulend, 1998; Malek and Izumo, 1995). Despite this importance, little is known about the general nature of the responses by cells to a given stress. Recent studies have characterized some of the responses of cells to mechanical stimuli, including determining local viscoelastic parameters (Bausch et al., 1998), studying mechanosensitive ion channel activation (Hu and Sachs, 1997; Sackin, 1995), and gene induction (Chaqour et al., 1999; Chiu et al., 1999; Khachigian et al., 1997), and considering cell geometry changes, for example, via focal adhesion shifting (Davies et al., 1994; Girard and Nerem, 1995; Kanda et al., 1993). Studies such as these indicate that the effects of mechanical forces are important in modeling cellular responses in many biomedical systems.

Typically, global stresses are applied uniformly over a large number of cells, either by fluid shear stress or by some form of membrane stretching (Brown et al., 1998). These techniques are not suitable, however, for studying individual cells or probing local cell membrane and cytoskeletal mechanics. Individual cell assays allow the determination of the statistical distribution in cell responses, in addition to the average value derived from assays using large populations. For example, a Northern blot combines the responses of several thousands to millions of cells to obtain a single readout. Using an individual cell assay provides a clearer idea of the nature of the response, differentiating between small global changes and drastic local changes (Brown et al., 1998; Davies, 1995; Davies et al., 1999).

Some techniques are available to examine the mechanical response of single cells. Pipetting technologies are used to locally deform cells, typically blood cells, to probe the membrane stiffness, and characterize the cells as they traverse narrow channels (Mow et al., 1994). Atomic force microscopy and optical traps are used to probe cellular and subcellular forces, such as those of kinesin motors (Block et al., 1990; Kuo and Sheetz, 1993). Magnetic traps with one pole (unipolar) can generate nanoNewton levels of force on beads attached to cells and have been used to probe the properties of cell membranes (Bausch et al., 1998). These techniques have limitations, such as low force generation (optical traps), the small number of cells that can be assayed at once, and the need to place cells carefully to assay them suspended for micropipette aspiration, or positioned with submicron precision to regulate the applied force in unipolar magnetic traps.

The generation of a uniform stress field based on a magnetic trap with multiple poles was first reported in 1996 (Amblard et al., 1996). Traps based on this design can generate a force with a small variance over a relatively large area, depending on the specific trap parameters. However, two major limitations in this type of trap are that the trap cannot typically exert much force, usually on the order of 10 pN per bead, and the tight trap geometry precludes the use of short-working-distance high-numerical-aperture objectives for high-resolution microscopy imaging. This paper presents the design of a two-photon micromanipulation workstation featuring a novel magnetic trap that can exert several hundred picoNewtons of force on micromagnetic

Submitted June 14, 2001, and accepted for publication January 14, 2002.
Address reprint requests to Dr. Peter So, Department of Mechanical Engineering, 77 Massachusetts Avenue, Rm 3-461A, Cambridge, MA 02139. Tel.: 617-253-6552; Fax: 617-258-9346; E-mail: ptso@mit.edu.

0006-3495/02/04/2211/13 $2.00

beads. The unique design of the trap, guided by electromagnetic finite-element simulations, optimizes the field magnitude while maintaining a uniform field gradient. The geometry of the trap accommodates a high numerical aperture microscope objective so that continuous, three-dimensional fluorescence images of the sample being stressed can be acquired before, during, and after the application of the force. This combination of the magnetic manipulator and imaging technology into a cell-mechanics workstation can be used to study the mechanical properties of cells, as well as a wide range of molecular responses based on different fluorescence reporters, such as those of ion channel activation, genetic induction, or cell migration. Further, by changing the surface proteins on the micromagnetic beads attached to the cells, specific membrane proteins can be targeted to examine certain receptor functions. In this study, the design of the magnetic trap/two-photon workstation is presented. The suitability of this workstation for studying cellular deformation is demonstrated by gauging the local versus global responses of the cells, with an emphasis on the three-dimensional, long-term (minutes) deformation patterns.

MATERIALS AND METHODS

Magnetic trap design

The design of the magnetic trap had to satisfy the following requirements. Geometrically, the trap has to fit on the stage of a two-photon microscope, while allowing the objective to move to within the working distance of the sample. The field exerted by the trap should result in a nearly uniform field gradient in a sample region large enough to contain many tens to hundreds of cells. The magnitude and direction of the force need to be adjustable, and the trap could not heat to the extent that cells die with a few minutes of exposure. The trap was developed to satisfy these requirements while maximizing the force that would be generated on a given micromagnetic bead.

Magnetic transducers exert forces on paramagnetic or ferromagnetic objects. Ferromagnetic materials have a permanent magnetic dipole moment and will experience a force in the presence of an external magnetic field gradient:

$$F = \frac{1}{2}\mu_0 \nabla (m \times H),$$

in which μ_0 is the permeability constant, m is the magnetization of the particle which is assumed to be uniform, and H is the external magnetic field strength. Although higher forces are typically generated with ferromagnetic particles due to their higher magnetization volume, they are more difficult to manipulate because these particles aggregate once magnetized. For some applications, super-paramagnetic beads can be applied more conveniently. By definition, super-paramagnetic systems lose their magnetization once the external field is removed. The typical magnetic susceptibility of these particles is on the order of unity in SI units. The force exerted on a super-paramagnetic particle is:

$$F = \mu_0 \chi V \nabla (H \times H),$$

in which χ is the volume susceptibility and V is the bead volume. The applied force increases with increasing field strength and increasing field gradient, up to the saturation of the transducer material in the ferromagnetic case and both the transducer and magnetic beads in the paramagnetic case.

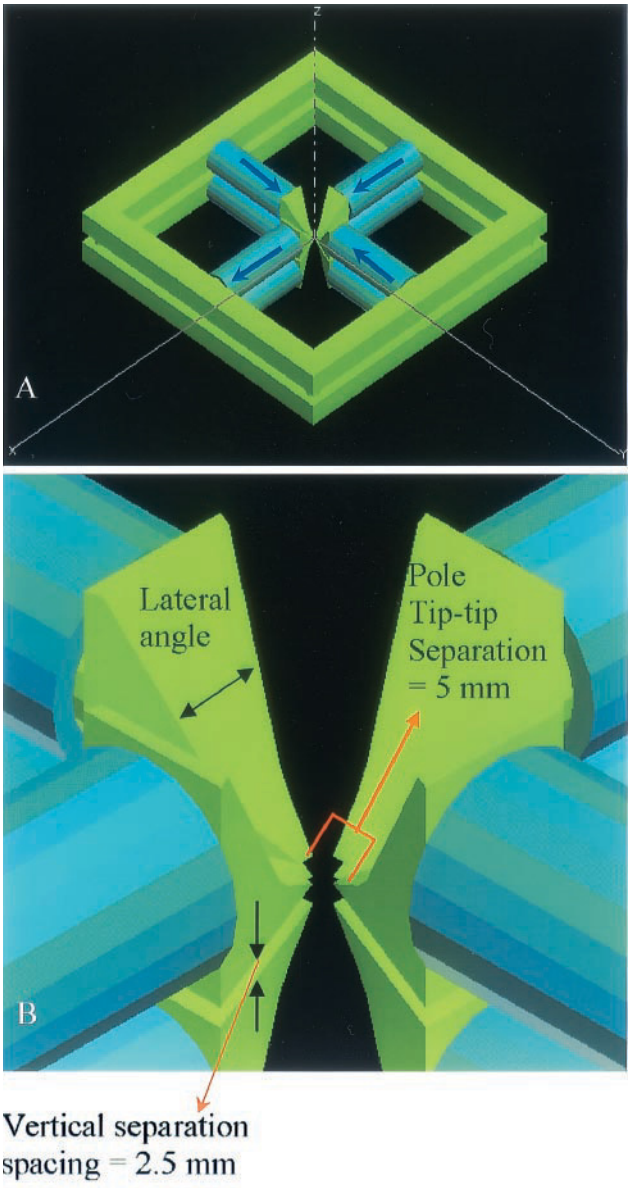

FIGURE 1 Schematic of the quadropole. (*A*) The backiron is the square iron connecting the four poles together. The tips converge to the center of the trap where the sample is placed. The two quadropoles are placed in a mirror image configuration with a 2.5-mm separation between them at the tips. The blue arrows indicate the direction of the magnetic flux along the poles. There are three flows into the sample region and one flow out. All currents are at the same magnitude for force generation. (*B*) Tip shape was primarily designed to fit a microscope objective. Other factors such as stability were also taken into account for the lateral dimensions.

The basic trap design for this study follows the work of Amblard et al. (1996) (Fig. 1). Enhancements to the design were guided in part by the electromagnetic simulation program Maxwell, from Ansoft (Pittsburgh, PA). This design consists of eight electromagnets (poles). Each pole is wrapped 550 times with a No. 24 gauge copper wire, turning the pole into an electromagnet. The pole material is CMI-C steel, which has a relatively high permeability and saturation. Whereas it is possible to use materials of

higher permeability and saturation (e.g., Hiperco 50), simulations indicated that for the intended current levels of a few amperes, there is no significant difference in field strength or gradient. The force levels are higher for higher saturation level materials at large currents, but at those currents the magnetic trap will quickly heat to temperatures inimical to cell function without active cooling. Active cooling was not implemented at this time, to minimize mechanical perturbations to the specimen. Further, permanent magnets were not used because they offer no easy way of precisely controlling or producing time-dependent variations in the force.

In the design presented in this study, the pole pieces are arranged in two *x-y* planes with four pole pieces each. The four in-plane pole pieces are set along the *x* and *y* axes, with the tips pointing toward the origin, where the specimen will be placed (Fig. 1 *A*). This location is denoted the sample region. This set of four poles forms a magnetic quadropole. Finite element simulation indicates that to use the field as efficiently as possible, the magnetic flux circuit must be completed. Thus, a backiron made from CMI-C rod was used to connect each set of four poles. The magnetic field in the sample region was compared for three possibilities: a magnetic trap with no backiron, with a backiron, and finally with triple-length poles and no backiron (to test the contribution of the extra material in the backiron). The mean field strength was significantly higher for the trap with a backiron arrangement (for field strength, 50%–100% higher than the triple length polar trap and >300% higher than the configuration without a backiron).

By altering the currents through these coils, the field can be changed, giving control of the force levels and directions. Instead of using four pair-wise linked poles similar to Amblard's design, the use of eight individual poles (the "octopolar" configuration) allows more flexible control over the field structure. This permits vertical force generation (force perpendicular to the microscope stage) as well as horizontal force in any planar direction. The generation of a planer field gradient and force used in these studies is achieved by directing the magnetic flux away from the center of the trap along one pair of poles and toward the center along the other three pairs.

Simulations indicated that pole tip spacing plays an important role in maximizing trap force level. The spacing between the tips of the poles for a quadropole was chosen to be the smallest possible, given certain constraints, to minimize field deterioration. This spacing was set at a distance of 5 mm, which still accommodates water immersion objectives with long working distances (for example, the Achro-plan 63×, 0.9 NA, 1.5-mm working distance or Achro-plan 100×, 1.0 NA, 1.0-mm working distance, Zeiss, Thornwood, NY). The distance between the two quadropoles was set to bring the tips 2.5 mm apart vertically. This distance was chosen partially to permit the insertion of the sample and partially based on finite-element analysis of a simplified model that indicated that a ratio of 1:2 of vertical-separation:pole-tip-separation would result in losses of field strength of ~10% to 15% (from the maximum in the plane of the tip), but that a separation of 1:1 would result in more severe losses of up to 40% to 50%. The vertical geometry of the tip was designed to fit the objective body, whereas the lateral angle was designed for stability (Fig. 1 *B*). Two lateral angles were tested, 50° and 90°, and the field strength did not change between these two angles when the tip-to-tip separation was kept constant. However, a 90° tip would be extremely short and thin, so the 50° tip was used in the design.

Finally, the trap was designed to be as large as possible (24 cm on a side) to maximize the field that could be generated. Although a significantly larger trap may produce a slightly higher field and generate more force, the loss of stability resulting from being larger than the microscope stage would be undesirable. Additionally, the simulations show that the trap poles are saturated in the tip and midpole regions, and thus increasing the size will lead to diminishing returns in increased force.

Calibration and characterization of the trap

To gauge the ability of the trap to produce a horizontal linear force, a calibration was performed at various current levels. Each pole is driven by current of the same amplitude, but the directions of the currents are different to produce the appropriate flux directions as specified in Fig. 1 *A*. This creates the necessary field gradient to generate a force.

Paramagnetic microspheres, 4.5-μm diameter from Dynal (Oslo, Norway), were used to perform the calibration. A bead is placed into a chambered gasket (Coverwell, Molecular Probes, Eugene, OR) with an aqueous solution of 80% sucrose, having a viscosity of 100 centistokes. The trap was turned on, and the steady-state velocity of the bead was measured using a custom particle-tracking program. Using Stokes' formula for low Reynolds numbers flow, it is possible to calculate the corresponding force on the beads. Briefly, Stokes' formula states that

$$F = 3\pi\mu VD,$$

in which μ is the dynamic viscosity of the fluid, V is the velocity of the bead at steady state, and D is the diameter of the bead. Reynolds number is given by

$$\mathrm{Re} = \frac{VD}{\upsilon},$$

in which ν is the kinematic viscosity. For our calibrations, the maximal velocity is 0.01 m/s with a bead diameter of 4.5 μm and a kinematic viscosity of 10^{-4} m^2/s. Thus, the maximal Reynolds number for our experiment is $4.5 \times 10^{-4} \ll 1$, so Stokes' formula applies. Similar experiments were performed using ferromagnetic microspheres (graciously donated by Dr. Ben Fabry, Harvard University, Cambridge, MA).

To measure magnetic field uniformity, the magnetic field distribution in the trap was measured using a direct current magnetometer (Alpha Lab Inc., Salt Lake City, UT) with a miniature Hall probe. The active area of the Hall probe has dimensions of 3 mm × 2.5 mm and a thickness of 0.7 mm. Because the sample space in the trap is only ~5 mm × 5 mm × 2.5 mm, the small size of the probe is critical. The measured field distribution is the actual field distribution convoluted by the probe active area. These measurements should be a reasonable representation of the actual field distribution, because the field distribution inside the sample space of the trap varies gradually (as observed in scaled models of the current trap and in the results of the Maxwell simulation).

Two-photon microscope

The instrumentation and design of a basic multiphoton microscope has been described in several previous publications (So et al., 1995, 1998). Briefly, the multiphoton excitation microscope design is based on a mode-locked Titanium-Sapphire laser (Mira 900, Coherent Inc., Palo Alto, CA). A Glan-Thomson polarizer is used to control the excitation power. The beam expanded laser light is directed into the microscope via a galvanometer-driven *x-y* scanner (Cambridge Technology, Watertown, MA). Images are generated by raster scanning the *x-y* mirrors. The excitation light enters the Zeiss Axiovert microscope (Zeiss Inc., Thornwood, NY) via a modified epiluminescence light path. The scan lens is positioned such that the *x-y* scanner is at its eye-point, whereas the field aperture plane is at its focal point. Because the objectives are infinity corrected, a tube lens is positioned to recollimate the excitation light. The scan lens and the tube lens function together as a beam expander that over fills the back aperture of the objective lens. The dichroic reflects the excitation light to the objective. The dichroic mirrors are custom-made short pass filters (Chroma Technology Inc., Brattleboro, VT) that maximize reflection in the infrared and transmission in the blue-green region of the spectrum. Typical image sizes range from 40 to 200 μm on a side. The objective axial position is driven by a piezo-motor interfaced to a computer. The typical image acquisition time is ~2 s for a single *x-y* plane.

The fluorescence emission is collected by the same objective and transmitted through the dichroic mirror along the emission path. An additional barrier filter is used to further attenuate the scattered excitation light

because of the high excitation intensity. Because two-photon excitation has the advantage that the excitation and emission wavelengths are well separated (by 300–400 nm), short pass filters such as 2 mm of the BG39 Schott glass filter (CVI Laser, Livermore, CA) eliminate most of the residual scatter with a minimal attenuation of the fluorescence. A descan lens is inserted between the tube lens and the photomultiplier tube (PMT) to recollimate the excitation and to ensure that the emission light strikes the photomultiplier tube at the same position, independent of scanner motion. The fluorescence signal at each pixel is detected by a R7400-P photomultiplier tube (Hamamatsu, Bridgewater, NJ), which is a compact single photon counting module with high quantum efficiency.

Bead protocol

Polystyrene beads, 0.5-μm diameter, from Duke Scientific (Palo Alto, CA), were coated with human plasma fibronectin (Gibco, Rockville, MD) based on passive adsorption. All centrifugations are at 18,000 $\times$ g for 5 min at 4°C. The beads were supplied at 1% (w/v). One milliliter of the beads was pelleted by centrifugation, then washed in 1 mL of sodium phosphate buffer (pH 7.3), and pelleted again. The beads were then resuspended in 950 μL of the sodium phosphate buffer and then transferred to a microcentrifuge tube containing 50 μL of human plasma fibronectin (stock at 1 mg/mL) and incubated at room temperature for 3 h to overnight while being lightly agitated. The beads were then pelleted, washed once with phosphate-buffered saline, and then resuspended in 1 mL of phosphate-buffered saline for the final solution. This solution was stored at 4°C until needed, at which time it was sonicated in a bath sonicator for 10 to 30 s.

The tosylactivation protocol for fibronectin coating the magnetic beads was performed according to manufacturer's instructions. Approximately 2 to 3 μL of the magnetic beads was used per coverslip, corresponding to approximately one million beads. Fibronectin was chosen because it forms strong bonds to cells, specifically binding the integrin units that link to the cellular cytoskeleton.

Cell culture

Eighteen-millimeter, size 2 glass coverslips were incubated in Hanks Balanced Salt Solution (Gibco) with fibronectin at 2 μg/mL overnight at 4°C. Human aortic smooth muscle cells were plated on fibronectin-coated coverslips at a density of 8,000 to 12,000 cells/cm^2. At 1 to 3 days after plating, the cells were incubated with 1 to 5 μL of the 0.5-μm blue-green fluorescent diameter polystyrene beads from Duke Scientific. Cell passages between two and six were used for all experiments. After polystyrene bead loading, the cells were placed in the incubator overnight, then loaded with fibronectin coated magnetic beads for 30 min at 37°C, and placed in the magnetic trap.

For the green fluorescent protein-actin experiments, the National Institutes of Health 3T3 fibroblasts were taken from passages 5 through 10 and plated on fibronectin-coated coverslips as described for the human smooth muscle cells. Twenty-four hours after plating, the cells were transfected with a GFP-actin plasmid (kindly provided by Dr. Richard Gilbert, Massachusetts Institute of Technology, Cambridge, MA) using the lipofectin protocol according to manufacturer's instructions (Gibco). One microgram of plasmid DNA and 4 μL of lipofectin reagent were placed in 1 mL of Opti-MEM media (Gibco) per well of a six-well plate. Cells were incubated in the transfection solution for 4 h at 37°C, and then 1 mL of Dulbecco's modified Eagle's medium with 10% fetal calf serum was added to the cells. The cells were then incubated overnight and washed the next day. Transfected cells were assayed in the following 2 or 3 days, using magnetic beads (2–3 μL) loaded 30 min before the experiment. One to 2 μL of the polystyrene beads were added at the same time as the magnetic beads to the GFP-actin cells.

Workstation usage to stress and image cells

A section of the specimen was identified that contained a cell with attached magnetic beads, and at least two polystyrene beads attached to the coverslip but not on the actual cell itself. The polystyrene beads serve as markers and are used to eliminate the residual specimen stage movement (~100 nm) during activation of the magnetic transducer. A three-dimensional image stack was then acquired using the two-photon microscope with a z-spacing of 0.2 μm and a x-y resolution of 512 by 512 pixels, with each pixel representing ~0.15 μm. This set of data is called the "before" images. The magnetic trap was then turned on, and a 1-min delay was instituted to allow the section to stabilize. The forces used in this study ranged from 50 to 120 pN. The three-dimensional stack was then recorded again, called the "after" images. Each data block took ~20 min to complete. All images were sampled at a finer scale than diffraction limited resolutions. The image blocks were postprocessed with a blind deconvolution program (AutoDeblur, Autoquant, Watervliet, NY) to further improve image resolution.

Using the polystyrene beads as markers, any solid body displacement and rotation of the coverslip can be eliminated by matching the polystyrene beads' positions in the "before" and "after" image stacks. Then, a cross-correlation program (Insight, TSI, St. Paul, MN) was used to determine local displacements. The program takes an interrogation region, a subsection of the "before" images, 128 pixels by 128 pixels, and calculates a cross-correlation factor with respect to the "after" images. By shifting the interrogation region in the x and y directions, the cross-correlation function is obtained for all possible displacements. The x and y shifts, which maximize the cross-correlation function, corresponds to the displacement. By choosing many interrogation regions over the entire "before" picture, a map of the displacements is obtained. The images were also qualitatively analyzed for cell deformation by examining the acquired cell images.

RESULTS

Magnetic transducer characterization

The performance of the trap is well predicted by the finite-element model. According to the simulations, when the trap is configured to generate forces along the x direction with pole currents set at 1 A, the x component of the B field in the center of the trap is 0.17 T and has a gradient of 0.5 T/cm (Fig. 2 *A*). The simulation is in excellent agreement with the actual field measurement; when driving the magnet with 1A of current, the x component of the magnetic field at the center of the trap was measured to be 0.15 T at the gap center with a gradient of 0.4 T/cm. These values agree with the results of the Maxwell simulation to within 25%. The variation of the x component of the magnetic field along the y and z axes is less than 2% within 500 μm from the trap center, and less than 10% within 1 mm of the trap center. This degree of variation is also in agreement with the Maxwell simulations. The field strengths at the four pole surfaces on the specimen plane are measured to be 0.072 $\hat{x}$ T, 0.095 $\hat{y}$ T, -0.095 $\hat{y}$ T, and 0.25 $\hat{x}$ T. These ratios are consistent with what is expected from the basic trap design (Amblard et al., 1996). The y and z components of the magnetic field vary less than 0.025 T within 250 μm from the trap center and less than 0.05 T within 500 μm. This level of magnetic field and gradient corresponds to negli-

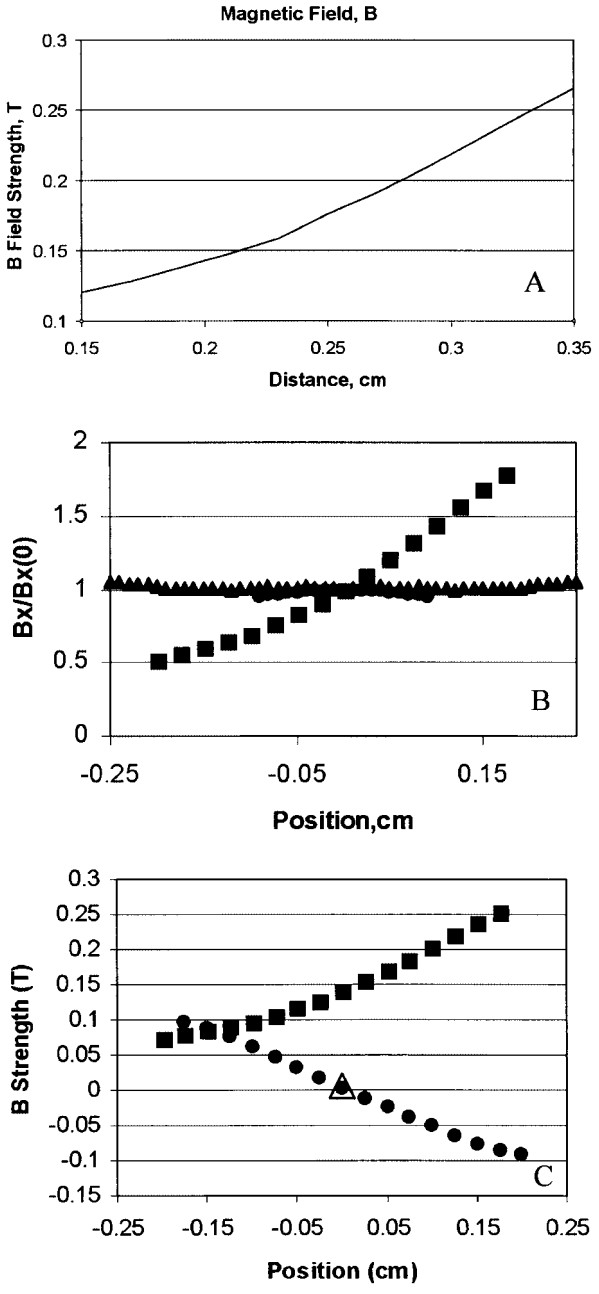

FIGURE 2 Electromagnetic simulation and Hall probe measurement results. (*A*) B field strength in the sample region, where 0.25 cm is the center of the trap. The field varies ~10% in the center 500 μm (0.225–0.275 cm) of the trap. The field gradient is very uniform in this region as well. (*B*) The *x* components of the magnetic field strength (B_x) is plotted as a function of distances from the trap center along *x* (*square*), *y* (*circle*), and *z* (*triangle*) directions. The plotted field strength is normalized to the maximal value at the trap center. (*C*) The *x* components of the magnetic field strength (B_x) is measured along *x* direction (*square*); the *y* components of the magnetic field strength (B_y) is measured along *y* direction (*circle*); the *z* components of the magnetic field strength (B_z) at the trap center is plotted (*triangle*). Due to geometric constraints of the trap, B_z can only be measured at trap center.

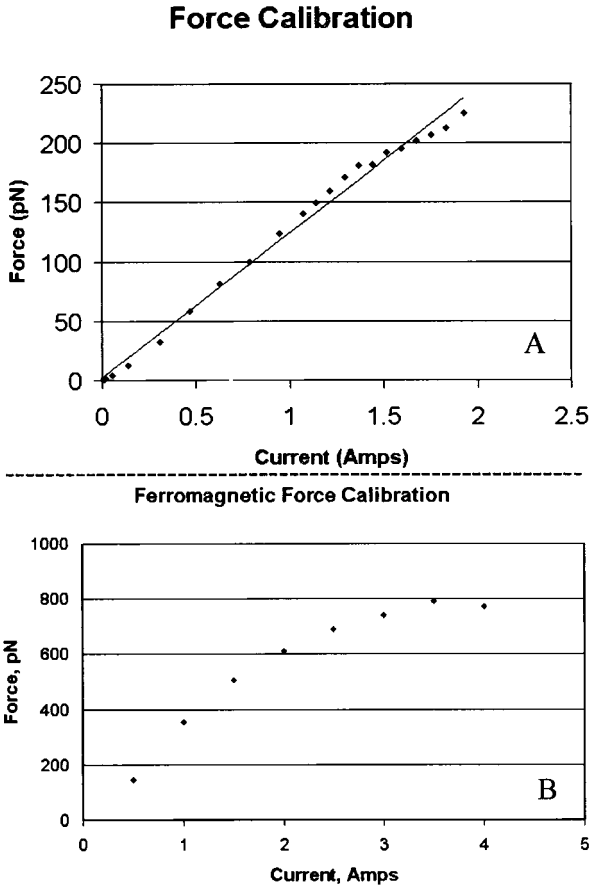

FIGURE 3 Calibration of the magnetic trap. The graphs show the calibration plots for (*A*) the super-paramagnetic beads and (*B*) for the ferromagnetic beads. The calibration in (*A*) also has a best fit line to illustrate the trend of the trap, and to show the effects of saturation at higher currents. These effects are clear in (*B*) as shown by the decrease in slope at higher currents.

gible forces along the *y* or *z* directions within 50 μm of the trap center. At a distance of 250 μm, the force in the *y* direction is at most 10% of the force along *x* direction and increases to less than 30% at a distance of 500 μm.

Other measurements indicate that the field gradient along the *x* axis is uniform and the magnitude of the field varies within $\pm$10% over a distance of 500 μm. This is also in good agreement with the Maxwell simulation (Fig. 2 *B*). If a cell takes up an area of 100 μm^2, a force that is constant to within 10% can be exerted on over 2500 cells simultaneously at full confluency. Finally, the *y* and *z* components of the magnetic field near the center of the sample section is very small in the respective *y* and *z* directions (Fig. 2 *C*). This indicates that there is little force in the *y* and *z* directions in the sample region.

The calibration reveals the range of forces that can be obtained using this trap. The force that can be obtained using super-paramagnetic beads is over 200 pN at 2 A driving current (Fig. 3 *A*). The force can be increased further using solid iron microspheres, where the force reached almost 800 pN with the application of 4 A of current (Fig.

3 *B*). The paramagnetic beads were not tested at 4 amps because saturation was evident at lower levels.

To test the suitability of the workstation to examine cells, a temperature test was performed. Under ambient conditions, the trap's temperature did not exceed 50°C at the poles and did not exceed 35°C in the sample region when the trap was operating at 100 pN for 1 h. Under forced convection conditions with a fan, the temperature at the sample region stayed at ~36° C for up to 4 h at 100 pN. Therefore, the temperature is not inimical to cell viability.

In our studies, we found that the poles developed a small but noticeable magnetization in the absence of current. Together with hysteresis effects, these changes will gradually alter trap characteristics. Although these effects are currently relatively small (on the order of a few picoNewtons), it can affect the accuracy of low force measurements. The future addition of feedback circuitry to the trap will help maintain long-term reproducibility of the force.

Measuring cellular three-dimensional deformation under focal stresses

The workstation was used to examine the response of cells to focally applied stresses. The study of cellular mechanical responses is an active research area. However, the effect of focal stresses on the three-dimensional architecture of the cell has not been closely examined. In addition, few studies have considered the moderate-to-long-term response of cells; most studies examine only the nearly instantaneous response of the cell to applied stresses. This workstation can collect data for either time interval.

Application of 50 pN is sufficient to show deformation in the cellular structure as determined by ingested beads (Fig. 4). The cell structure shows an apparent stretching and rotation. Curiously, the stretching is almost perpendicular to the direction of the applied force. At larger forces (120 pN), the global stretching and rotation are even more evident, and the development of a large local deformation near the location of the magnetic bead becomes evident (Fig. 4). The global deformation can be quantified using a cross-correlation algorithm, which yields displacement vectors based on analysis of an interrogation region 128 by 128 pixels (Fig. 5). While the resolution of the vectors is not optimal, using this method allows the generation of a displacement map with subcellular resolution. The length and direction of the vectors represents the most probable displacement at a particular cellular location. The magnitudes of local cell deformation are quantified and can be used to calculate cell stretching and rotation. The vectors increase in size from the bottom of the image to the top, indicating that the displacements are increasing in magnitude. In addition, the displacement vectors exhibit a nonuniform horizontal component, indicating that the cell has rotated. We quantified the magnitude of the displacement vectors throughout the cell in a histogram, which shows the frequency distributions of the vector's x and y components (Fig. 5, *B* and *C*). The large bias toward positive y displacements and the relatively balanced contributions from positive and negative x components is consistent with the observation that the cell is stretching and rotating. Clearly, quantitative information can be obtained from the cross-correlation vectors.

Over a period of 20 to 30 min required to acquire the data, it is possible that the cell has migrated or significantly remodeled itself even without any forces on the cell. To test this hypothesis, a "before" three-dimensional image block was acquired of another cell, and the sample holder was then gently tapped to create a global translation and rotation without actually stressing the cell, and the "after" image block was then acquired. The image-blocks were processed and shows minimal or no displacements at all (Fig. 6). A histogram of displacement vector of this cell is also presented (Fig. 6, *D* and *E*). Although this data was taken at one-half the resolution of the previous data set, cross-correlation analysis shows that the displacement vectors in the nonstressed cell image are at approximately a factor of three smaller than those of the stressed cell, and these vectors are located predominantly off the cell itself, possibly corresponding to diffusing debris in the specimen. A second test was performed where a cell with no magnetic beads attached to it was placed in the magnetic trap, a "before" data clock acquired, and the trap activated to produce 120 pN of force. The "after" data block was then acquired and compared with the before. No significant changes in cell shape or location was present (data not shown). These results suggest that without an applied force, the cell does not migrate or remodel to the same extent as under a mechanical stress. The magnetic field, vibrations from operating the trap, and the temperature effects from the trap do not result in a significant change in cell morphology. When the trap was turned off, the cell remained viable for further studies, as seen in Fig. 4, where Fig. 4 *C* was acquired after the trap was turned off from Fig. 4 *B*. However, no specific long-term data were gathered on the possible recovery of the cell for this study.

Because the images form a complete three-dimensional block of data, the deformation can be visualized from a different perspective. Images reconstructed in the vertical planes show that the deformation is not limited to the surface (Fig. 7). The largest deformations are somewhat limited to the upper one-half of the cell, but they pervade the cell to the nucleus.

The magnetic trap and two-photon setup was also used to examine GFP-actin movement in 3T3 fibroblasts as well (Fig. 8). These data represent more direct evidence of intracellular deformation. The response of the cells to a focal force involves the cytoskeleton and that the nuclear shape also changes, despite being far from the magnetic bead.

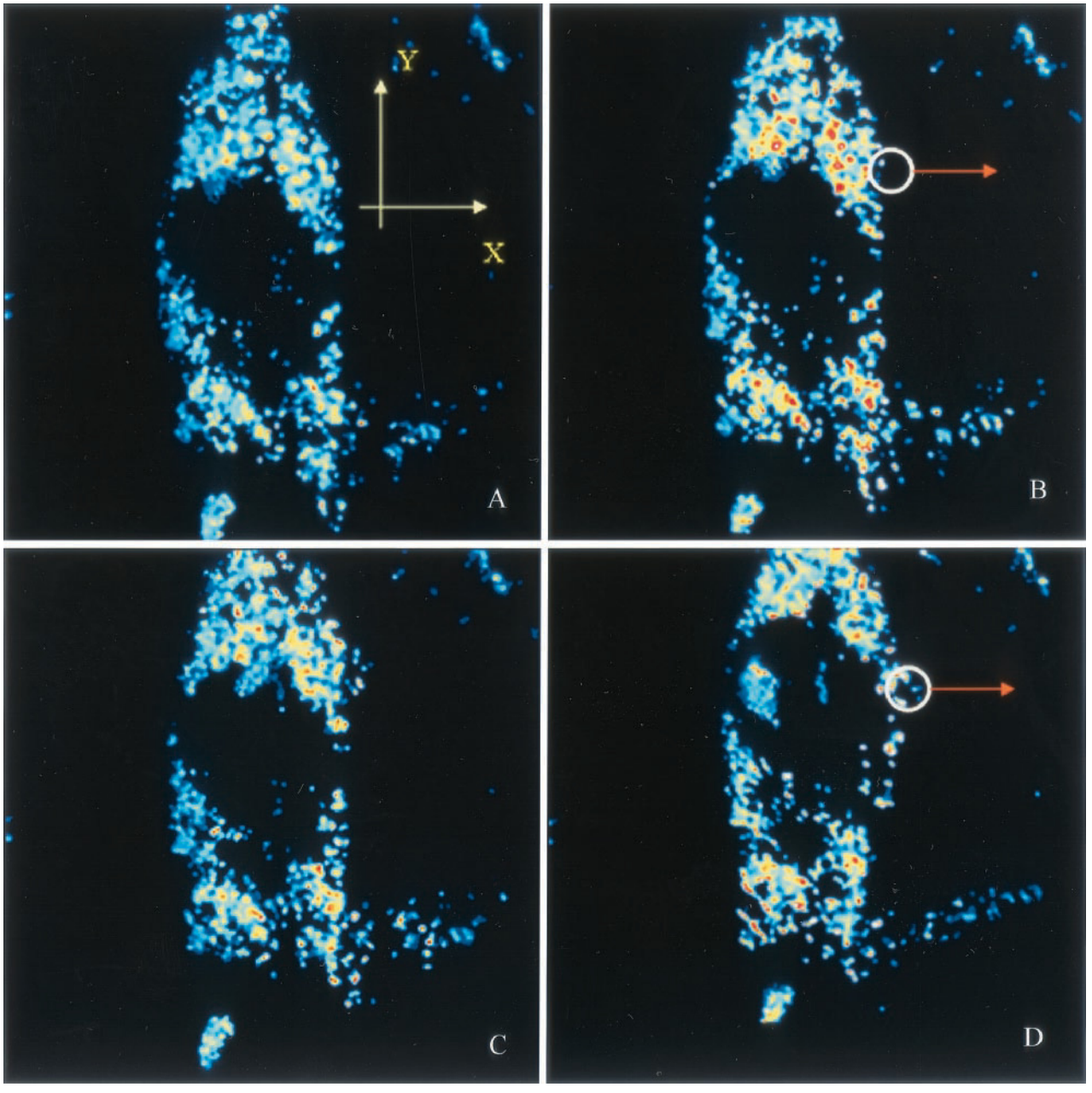

FIGURE 4 Deformation of a smooth muscle cell. The two-photon images show (*A*) a cell in its resting state, and (*B*) under 50-pN force (low force) from a single magnetic bead attached at the location shown by the small white circle in the direction depicted by the orange arrow. The cell under force is slightly rotated in the clockwise direction and is also slightly longer in a direction perpendicular to the applied force. The entire image size is 500 × 500 pixels. Each pixel corresponds to 0.15 μm. The two-photon images of the same cell as in *A* and *B*, shown in *C* a resting state, and *D* under 120 pN of force (high force) from the same magnetic bead (in the same direction). The deformation is more apparent in this case, as is a local pinching near the location of the attached bead. The cell also noticeably thins in the direction of the applied force, excepting the area near the pinching.

DISCUSSION

A magnetic micromanipulator capable of producing uniform forces on the order of a few hundred picoNewtons over an area of 500 × 500 μm^2 was designed. This micromanipulator is integrated with a high-resolution two-photon microscope so that three-dimensional images of deformation fields in biological specimens could be taken and analyzed. This two-photon micromanipulation workstation provides a robust way to study structural, biochemical, and genetic changes in biological systems with three-dimensional resolution.

The magnetic trap allows precise control of the magnitudes, directions, and frequencies of forces produced. The

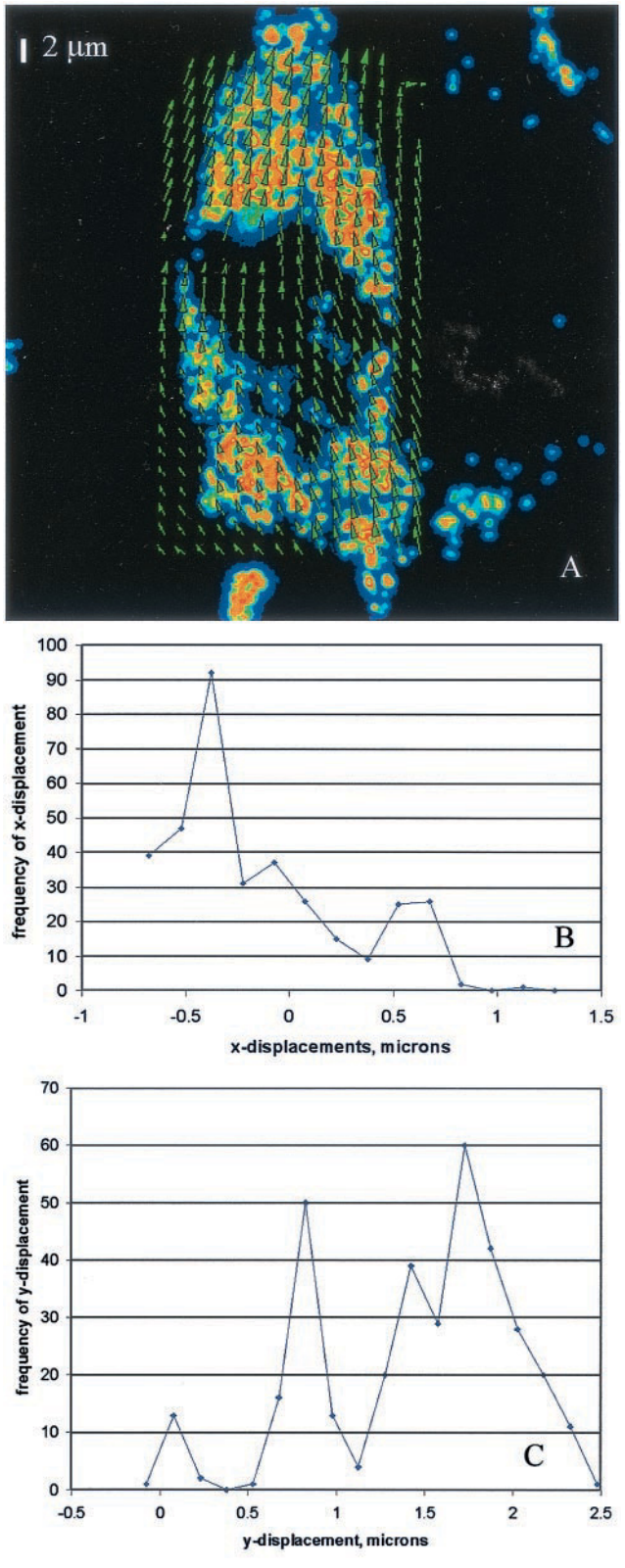

FIGURE 5 Cross-correlation analysis of the low force deformation. (*A*) The 50 pN "before" and "after" data were processed by a cross-correlation program with interrogation regions 128 by 128 pixels. The vectors lengthen in the *y* direction, indicating that the cells is elongating, and also show a *x* component that changes from negative to positive as *y* increases. This means that the cell is also rotating or twisting in response to the applied stress. The bar indicates the length of a 2-μm displacement vector in the *y* direction. These 350 vectors are decomposed into frequencies of the (*B*) *x* displacements and (*C*) *y* displacements. Thus, the histograms provide a simple way of determining which direction the cell is displacing predominantly (the positive *y* direction in this case) and by how much (10–15 pixels, or ~2 μm).

force magnitude generated is over an order of magnitude larger than previous designs that can produce a uniform field over a large area. While a single pole magnetic manipulator such as the one designed by Bausch et al. (1998) can produce forces up to tens of nanoNewtons, the distance between the pole and the magnetic particle has to be regulated to within a few microns to obtain an accurate knowledge of the applied forces. Single pole manipulators are more appropriate for problems where the induced movement of the particle is small, for example, in the case of cell membrane studies. However, uniform field devices can provide more accurate force controls in studies where the magnetic particle may be induced to move distances of over several microns, such as in the global, stress-induced, cellular motion observed in this study, and in force spectroscopy studies of biopolymers that are significantly longer than its persistent length.

Unlike the single pole devices where only local forces can be generated, this transducer can produce uniform forces over an extended area. This feature is vital for studying many problems in cell mechanics, where the responses of many cells must be averaged to obtain statistically relevant results. Some examples include the study of calcium flux of mechano-activated channels and mechanically activated gene induction. The statistical nature of these processes requires the study of a large number of cells. This transducer generates a nearly uniform magnetic field over a $500 \times 500\ \mu m^2$ area allowing the simultaneous manipulation of over a thousand cells. The individual responses of all the cells can then be assayed microscopically. This way, both the average response and the statistical distribution information of the cell population can be obtained.

However, the generation of a uniform field over a large area has some disadvantages. One concern is that many cellular mechanical responses depend on the history of forces exerted on the cells. For example, local stiffening of integrin-cytoskeleton linkages and cytoskeletal rearrangement under external forcing have been observed (Choquet et al., 1997; Glogauer et al., 1997). After studying the responses of a given cell under magnetic manipulation, it is possible that the neighboring cells will respond differently. This effect is less of a concern for single pole traps, because the stress field decreases rapidly away from the pole tip.

An important future development involves improving mechanical stability of this trap. When the trap is toggled on/off, there is a noticeable movement in the sample section

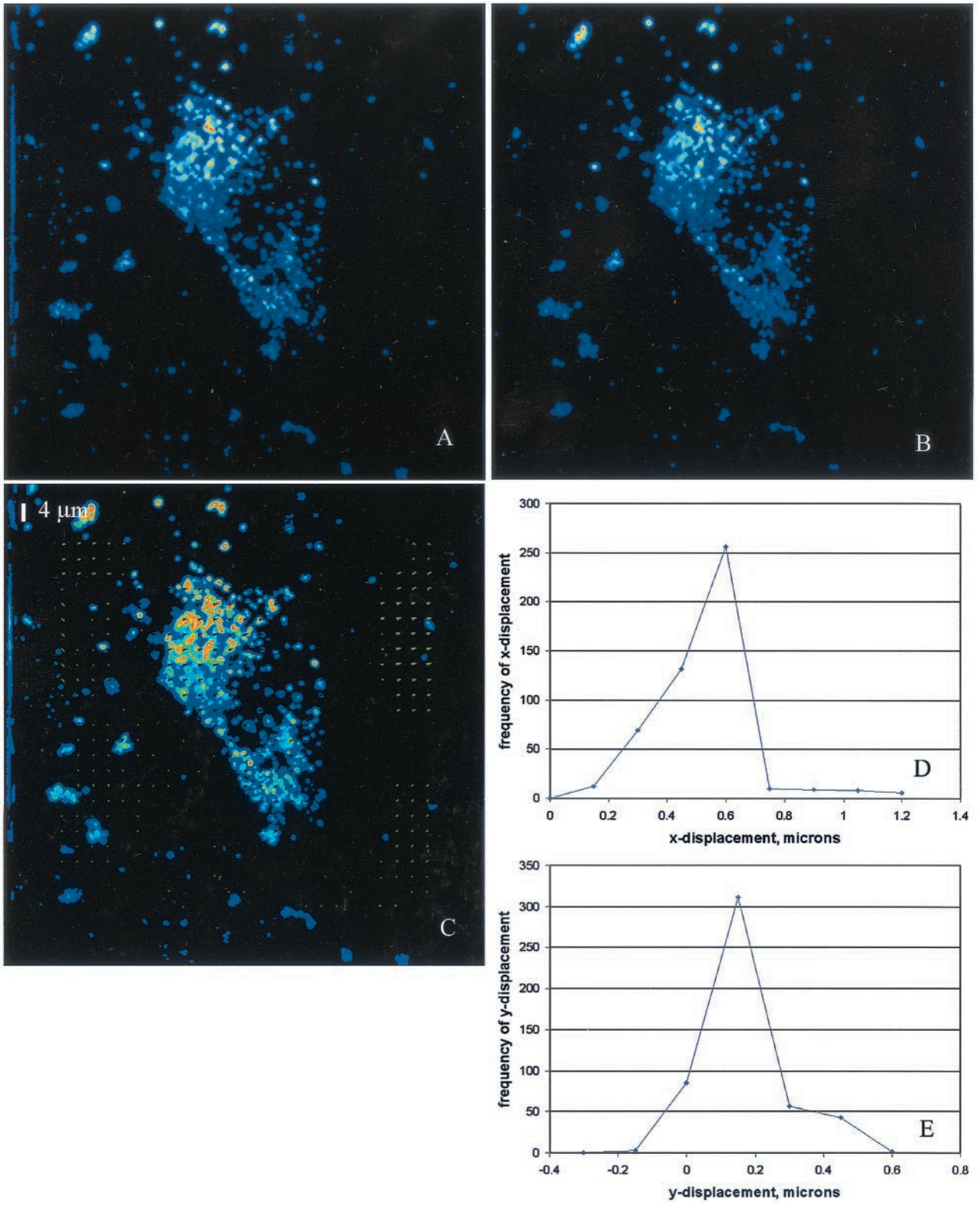

FIGURE 6 Control specimen with no applied force. The two-photon images show (*A*) the before and (*B*) after images of the same cell, with a manual perturbation of the sample holder. The two-photon image (*C*) shows the same cross-correlation analysis as done for Fig. 5. The vectors are shown at twice their normal size. There are no displacements in the actual cell, and only trace displacements in the vicinity of the cell, validating the cross-correlation algorithm, and the programming used to correct for rigid body displacements and rotations. The bar indicates the length of a 4 μm displacement vector in the *y* direction. These vectors are decomposed into frequencies of the (*D*) *x* displacements and (*E*) *y* displacements similar to those of Fig. 5. Note the much smaller magnitudes of *y* displacements.

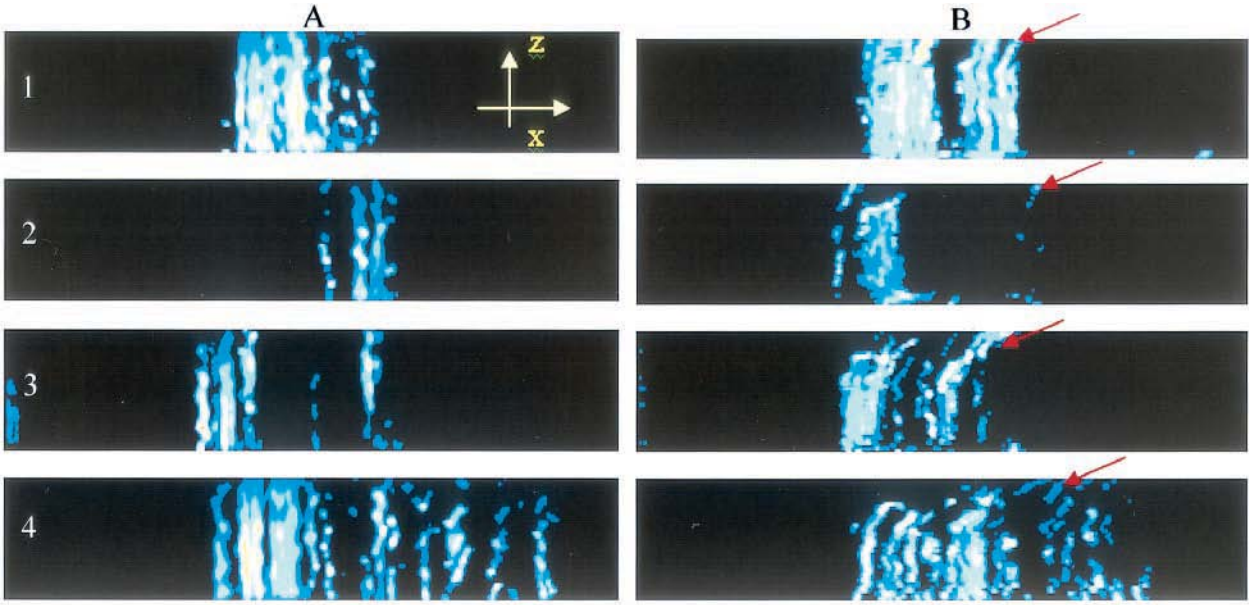

FIGURE 7 Vertical slice of a cell before and after stress is applied. These reconstructed two-photon images are taken from the same data set as used for Fig. 4 (120 pN). The vertical direction is the *z* axis, representing the axis parallel to gravitation. The top of the cells appears flat because the images were truncated. These images show slices at (1) 50, (2) 150, (3) 250, and (4) 350 pixels from the top of the image in Fig. 4, *C* and *D*. The cell deformation (indicated by *red arrows*) is clearly in the direction of the applied stress, and while this deformation is mostly limited at the top one-half of the cell, it also clearly penetrates the cell to the nucleus.

as viewed through the microscope (on the order of a hundred nanometers). This stability problem may be addressed in the future by the introduction of support struts, or by local encasements of the trap joints in plastic or epoxy. If the trap is intended for repeated uses, fatigue may result and can cause the trap force to change with time. For this study, the

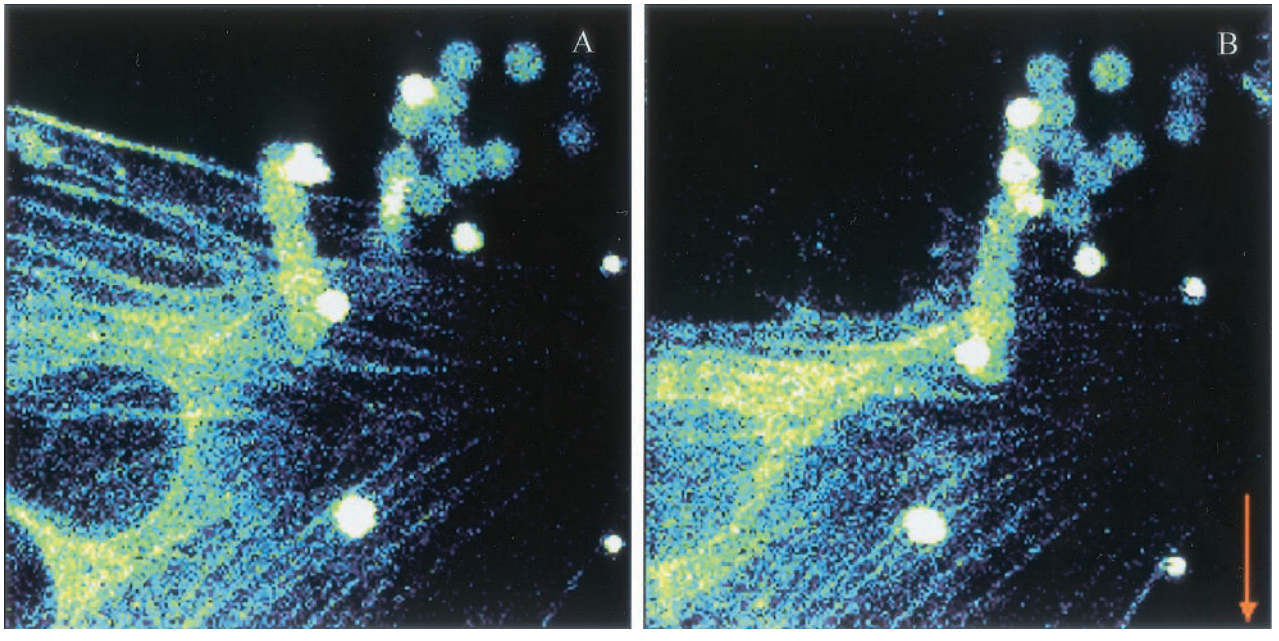

FIGURE 8 Deformation as visualized by GFP-actin transfected 3T3 cells. The two-photon images show the (*A*) before and (*B*) after images of NIH 3T3 cells transfected with GFP actin. The stress fibers are clearly visible, and the upper fibers collapse to a thick bundle upon application of 150 pN per bead. The direction of the force is indicated by the orange arrow, and there is almost 1 nN total force on the cell. The beads are also visible as dimly fluorescent spheres in the upper right hand corner of the images. The nucleus also changes shape from an oval to a more eccentric ellipse upon the application of the force.

solid body displacement has been corrected by attaching latex particle to the coverslip as reference points.

We believe that this workstation is a very useful device for furthering the understanding of cell mechanics. Predicting the cellular responses to mechanical stimulus requires the development of theoretical models that quantify the cellular mechanical and structural modifications in response to external forces. Two of the leading theories include the tensegrity model and the open-cell foam model (Ingber, 1993, 1997; Satcher et al., 1997; Satcher and Dewey, 1996; Stamenovic and Coughlin, 1999; Stamenovic and Coughlin, 2000). These continuum models can be used to predict cellular bulk modulus. Equally importantly, these models summarize a number of the qualitative observations of how cells responses to mechanical stimulus such as the stress dependent increase in cytoskeletal stiffness (Wang et al., 1993; Wang and Ingber, 1994). In terms of experimental verification, innovative techniques such as twisting magnetic cytometry (Wang et al., 1993), micropipette aspiration (Hochmuth 2000), microplate manipulation (Thoumine et al., 1999), and atomic force microscopy (Mathur et al., 2000; Rotsch and Radmacher, 2000) allow the cellular bulk modulus to be measured and provide comparison to existing theories. While these continuum models provide reasonable quantification of bulk cell properties, the effects of mechanical stimulus on intracellular structural rearrangement is less well understood. Stress-induced modification in intracellular structures and organelle conformation has been implicated in the activation of pressure sensitive channels (Davies et al., 1997; Glogauer et al., 1997; Pommerenke et al., 1996; Wu et al., 1999), modulation of gene activation (Lundberg et al., 1995; Lyall et al., 1994; Reusch et al., 1996; Songu-Mize et al., 1996; Wagner et al., 1997; Wilson et al., 1993), and regulation of protein posttranslation modifications (Hering, 1999; Liu et al., 1999; Mourgeon et al., 1999; Noubhani et al., 1996; Parsons et al., 1999). Significant challenges remain in extending existing theories to describe intracellular structural changes on the microscopic level taking into account additional factors, such as mechanical heterogeneities in intracellular components, cell-surface adhesion forces, and cell-cell interactions. Experimentally, the quantification of cellular structural rearrangement requires imaging methods capable of mapping intracellular strain field in three-dimensional on the subcellular level. Techniques, such as two-dimensional single particle tracking (Bausch et al., 1998, 1999) and laser tracking microrheology (Yamada et al., 2000), glass needle cell poker (Petersen et al., 1982), and atomic force microscopy (Mathur et al., 2000; Rotsch and Radmacher, 2000) allow cellular mechanical properties to be determined locally at selected locations. Extending these studies to map intracellular strain fields in three-dimensional represents an important next step. Based on three-dimensional image deconvolution, intracellular strain fields have been mapped in the presence of fluid flow (Helmke et al., 2000). The development of the two-photon magnetic manipulator workstation represents a powerful alternative method to map the three-dimensional intracellular strain field in almost real time, while providing a method to exert directed local deformation fields with precise control.

As an evaluation of the capability of this system to quantify the distribution of intracellular deformation, human aortic smooth muscle cells with endocytosed polystyrene beads were studied with and without forces applied on them. Unlike previous studies where cellular deformation resulting from local stress is measured at a few selected points, this study allows the deformation vectors to be mapped throughout most of the cell volume except at regions where the endocytosed particles are excluded, such as the nucleus. The ability to measure deformation vectors throughout the majority of the cell volume allows us to visualize the cellular responses to mechanical stimuli in three dimensions. Even when the applied stress is planar and is generated at a single focal location, we found that cellular deformation occurs in all three dimensions. Different projections of the three-dimensional reconstruction of the data indicate that the deformations are not restricted to the surface—they extend through the cytoplasm to the nucleus. Similar results were observed in flow induced cytoskeletal deformation in endothelial cells (Helmke et al., 2001). Preliminary data support the notion that the nucleus itself changes shape when a stress is applied on the cell, which is consistent with a step-strain analysis done by Ingber et al. (Bojanowski et al., 1998; Maniotis et al., 1997). However, this data suggests that the nuclear deformation could be induced by global continuum cellular changes as well as fibrous interconnections between the cell membrane and nucleus. These results demonstrate the need for analyzing the entire architecture of the cell, and not just a two-dimensional projection, if a complete cell model is to be attained.

More in-depth examination of the displacement field provides other interesting observations. There are displacements of intracellular structure along the stress direction in the local vicinity (within a 10-μm range) around the magnetic bead. The magnitude of this displacement is less than 1 μm for force magnitudes less than 200 pN. A number of cells, approximately one-half of the cells examined, are observed to further lengthen globally in a direction almost perpendicular to the direction of applied force on a time scale of minutes (e.g., Fig. 5). The magnitudes of these global motions are relatively large and are on the order of 1 to 10 μm for force magnitudes less than 200 pN. It is interesting to compare our results with previous studies (Bausch et al., 1998) using similar methods and force magnitudes under dynamic loading with a bandwidth on the order of seconds. These studies observed similar localized displacements approximately along the stress direction with magnitude comparable with the local displacement observed in our study. In our static loading study, it is clear

that global displacements becomes the dominant response mechanism on a time scale of minutes. These global motions are likely to be caused by physical processes that are different from those that generate the smaller, more instantaneous local displacements. One may postulate that these global displacements may involve active processes such as cellular cytoskeleton remodeling or focal adhesion shifting (Mathur et al., 2000). Clearly, further studies with more cells and cell types will help yield a deeper understanding of the cell responses. Such studies might include statistical analysis to quantify the bulk modulus variances over a population of cells. Statistical analysis will be needed to take account of variables such as bead location, cell orientation, and cell-cell contact.

Although the visualization of endocytosed particles has been commonly used to study cell mechanics, the correlation between the distributions of these ingested polystyrene beads and the cytoskeletal components is not well characterized. The active and passive processes involved in cellular deformation under applied stress can be better understood by directly visualizing major cellular structures responsible for the maintenance and modification of cell shapes, such as actin stress fibers, microtubules, and focal adhesion complexes. As a first step, this workstation was used to probe the responses of GFP-actin expressing fibroblasts to mechanical stresses. The actin stress fibers clearly showed a dramatic remodeling in response to the applied forces. Again, nuclear deformation was evident in these cells, indicating that the nuclear deformation induced by extracellular stress is a general feature of many cell types as observed in smooth muscle cells and fibroblasts in this report and in endothelial cells in previous studies (Bojanowski et al., 1998; Maniotis et al., 1997). This study with GFP-actin clearly indicates that the global deformation observed involves significant reconfiguration of the cytoskeleton structure. The collapse of a significant portion of the cell under stress (Fig. 8) suggests that the surface connections of a number of focal adhesion sites were severed. With the incorporation of video rate two-photon imaging capability into this workstation, it may be possible to directly track both short- and long-term stress-induced changes in actin filaments, as well as microtubules or other cellular structural components.

The two-photon magnetic-trap workstation is suitable for studying a variety of force-response behavior in biology. An immediate extension of the current work is study the effect of mechanical stresses on endothelial cells. Because the force is generally applied in a direction parallel to the substrate to which the cell is attached, the simulation of shear stress is easily achieved. Thus, it is possible to study the classical responses of endothelial cells to controlled shear stresses, such as looking at intracellular calcium concentration changes, focal adhesion shifting, and cytoskeletal rearrangement at the same time as the stress is being applied, rather than at discrete time points (Davies et al., 1997). Another possible application of this technique is the use of this device to study three-dimensional rheological properties of biopeptide gels that are finding uses in areas such as tissue engineering.

It is possible that the generated magnetic field itself can cause biological effects when cells are being studied. Magnetic field responses of biological systems have not been well-characterized, so detailed studies with a workstation such as the one presented needs to include controls to eliminate the effects of the field. However, it is clear this workstation provides the capabilities to systematically study the cellular mechanical response to establish a more comprehensive model of cell mechanics and behavior, and that this workstation is well suited for such an application. This workstation demonstrated that it can generate large, uniform forces over a large area as designed and when used in conjunction with two-photon microscopy was capable of generating detectable deformation in living cells.

This work was supported under the Whitaker Foundation and the MIT Center for Bioengineering grant number 2897700. Thanks to Dr. Richard Gilbert for sharing the GFP-actin plasmids used in this study and to Dr. Ben Fabry for sharing the ferro-magnetic beads used in this project.

REFERENCES

Amblard, F., B. Yurke, A. Pargellis, and S. Leibler. 1996. A magnetic manipulator for studying local rheology and micromechanical properties of biological systems. *Biophys. J.* 67:818–827.

Bausch, A. R., W. Moller, and E. Sackmann. 1999. Measurement of local viscoelasticity and forces in living cells by magnetic tweezers. *Biophys. J.* 76:573–579.

Bausch, A. R., F. Ziemann, A. A. Boulbitch, K. Jacobson, and E. Sackmann. 1998. Local measurements of viscoelastic parameters of adherent cell surfaces by magnetic bead microrheometry. *Biophys. J.* 75: 2038–2049.

Block, S. M., L. S. Goldstein, and B. J. Schnapp. 1990. Bead movement by single kinesin molecules studied with optical tweezers. *Nature.* 348: 348–352.

Bojanowski, K., A. J. Maniotis, S. Plisov, A. K. Larsen, and D. E. Ingber. 1998. DNA topoisomerase II can drive changes in higher order chromosome architecture without enzymatically modifying DNA. *J. Cell Biochem.* 69:127–142.

Brown, T. D., M. Bottlang, D. R. Pedersen, and A. J. Banes. 1998. Loading paradigms–intentional and unintentional–for cell culture mechanostimulus. *Am. J. Med. Sci.* 316:162–168.

Burger, E. H., and J. Klein-Nulend. 1998. Microgravity and bone cell mechanosensitivity. *Bone.* 22:127S–130S.

Chaqour, B., P. S. Howard, and E. J. Macarak. 1999. Identification of stretch-responsive genes in pulmonary artery smooth muscle cells by a two arbitrary primer-based mRNA differential display approach. *Mol. Cell Biochem.* 197:87–96.

Chiu, J. J., B. S. Wung, H. J. Hsieh, L. W. Lo, and D. L. Wang. 1999. Nitric oxide regulates shear stress-induced early growth response-1: expression via the extracellular signal-regulated kinase pathway in endothelial cells. *Circ. Res.* 85:238–246.

Choquet, D., D. P. Felsenfeld, and M. P. Sheetz. 1997. Extracellular matrix rigidity causes strengthening of integrin- cytoskeleton linkages. *Cell.* 88:39–48.

Davies, P. F. 1995. Flow-mediated endothelial mechanotransduction. *Physiol. Rev.* 75:519–560.

Davies, P. F., K. A. Barbee, M. V. Volin, A. Robotewskyj, J. Chen, L. Joseph, M. L. Griem, M. N. Wernick, E. Jacobs, D. C. Polacek, et al.,. 1997. Spatial relationships in early signaling events of flow-mediated endothelial mechanotransduction. *Annu. Rev. Physiol.* 59:527–549.

Davies, P. F., D. C. Polacek, J. S. Handen, B. P. Helmke, and N. DePaola. 1999. A spatial approach to transcriptional profiling: mechanotransduction and the focal origin of atherosclerosis. *Trends Biotechnol.* 17: 347–351.

Davies, P. F., A. Robotewskyj, and M. L. Griem. 1994. Quantitative studies of endothelial cell adhesion: directional remodeling of focal adhesion sites in response to flow forces. *J. Clin. Invest.* 93:2031–2038.

Girard, P. R., and R. M. Nerem. 1995. Shear stress modulates endothelial cell morphology and F-actin organization through the regulation of focal adhesion-associated proteins. *J. Cell Physiol.* 163:179–193.

Glogauer, M., P. Arora, G. Yao, I. Sokholov, J. Ferrier, and C. A. McCulloch. 1997. Calcium ions and tyrosine phosphorylation interact coordinately with actin to regulate cytoprotective responses to stretching. *J. Cell Sci.* 110:11–21.

Helmke, B. P., R. D. Goldman, and P. F. Davies. 2000. Rapid displacement of vimentin intermediate filaments in living endothelial cells exposed to flow. *Circ. Res.* 86:745–752.

Helmke, B. P., D. B. Thakker, R. D. Goldman, and P. F. Davies. 2001. Spatiotemporal analysis of flow-induced intermediate filament displacement in living endothelial cells. *Biophys. J.* 80:184–194.

Hering, T. M. 1999. Regulation of chondrocyte gene expression. *Front Biosci.* 4:D743–D761.

Hochmuth, R. M. 2000. Micropipette aspiration of living cells. *J. Biomech.* 33:15–22.

Hu, H., and F. Sachs. 1997. Stretch-activated ion channels in the heart. *J. Mol. Cell Cardiol.* 29:1511–1523.

Ingber, D. E. 1993. Cellular tensegrity: defining new rules of biological design that govern the cytoskeleton. *J. Cell Sci.* 104:613–627.

Ingber, D. E. 1997. Tensegrity: the architectural basis of cellular mechanotransduction. *Annu. Rev. Physiol.* 59:575–599.

Kanda, K., T. Matsuda, and T. Oka. 1993. Mechanical stress induced cellular orientation and phenotypic modulation of 3-D cultured smooth muscle cells. *Asaio J.* 39:M686–M690.

Khachigian, L. M., K. R. Anderson, N. J. Halnon, M. A., Jr. Gimbrone, N. Resnick, and T. Collins. 1997. Egr-1 is activated in endothelial cells exposed to fluid shear stress and interacts with a novel shear-stress-response element in the PDGF A- chain promoter. *Arterioscler. Thromb. Vasc. Biol.* 17:2280–2286.

Kuo, S. C., and M. P. Sheetz. 1993. Force of single kinesin molecules measured with optical tweezers. *Science.* 260:232–234.

Liu, M., A. K. Tanswell, and M. Post. 1999. Mechanical force-induced signal transduction in lung cells. *Am. J. Physiol.* 277:L667–L683.

Lundberg, M. S., D. N. Sadhu, V. E. Grumman, W. M. Chilian, and K. S. Ramos. 1995. Actin isoform and alpha 1B-adrenoceptor gene expression in aortic and coronary smooth muscle is influenced by cyclical stretch. *In Vitro Cell Dev. Biol. Anim.* 31:595–600.

Lyall, F., M. R. Deehan, I. A. Greer, F. Boswell, W. C. Brown, and G. T. McInnes. 1994. Mechanical stretch increases proto-oncogene expression and phosphoinositide turnover in vascular smooth muscle cells. *J. Hypertens.* 12:1139–1145.

Malek, A. M., and S. Izumo. 1995. Control of endothelial cell gene expression by flow. *J. Biomech.* 28:1515–1528.

Maniotis, A. J., C. S. Chen, and D. E. Ingber. 1997. Demonstration of mechanical connections between integrins, cytoskeletal filaments, and nucleoplasm that stabilize nuclear structure. *Proc. Natl. Acad. Sci. U. S. A.* 94:849–854.

Mathur, A. B., G. A. Truskey, and W. M. Reichert. 2000. Atomic force and total internal reflection fluorescence microscopy for the study of force transmission in endothelial cells. *Biophys. J.* 78:1725–1735.

Mourgeon, E., J. Xu, A. K. Tanswell, M. Liu, and M. Post. 1999. Mechanical strain-induced posttranscriptional regulation of fibronectin production in fetal lung cells. *Am. J. Physiol.* 277:L142–L149.

Mow, V. C. G. F., R. Tran-Son-Tay, and R. M. Hochmuth. 1994. Cell Mechanics and Cellular Engineering. Springer Verlag, New York.

Noubhani, A. M., S. Sakr, M. H. Denis, S. Delrot. 1996:Transcriptional and post-translational control of the plant plasma membrane H(+)-ATPase by mechanical treatments. *Biochim. Biophys. Acta.* 1281:213–219.

Parsons, M., E. Kessler, G. J. Laurent, R. A. Brown, and J. E. Bishop. 1999. Mechanical load enhances procollagen processing in dermal fibroblasts by regulating levels of procollagen C-proteinase. *Exp. Cell Res.* 252:319–331.

Petersen, N. O., W. B. McConnaughey, and E. L. Elson. 1982. Dependence of locally measured cellular deformability on position on the cell, temperature, and cytochalasin B. *Proc. Natl. Acad. Sci. U. S. A.* 79: 5327–5331.

Pommerenke, H., E. Schreiber, F. Durr, B. Nebe, C. Hahnel, W. Moller, and J. Rychly. 1996. Stimulation of integrin receptors using a magnetic drag force device induces an intracellular free calcium response. *Eur. J. Cell Biol.* 70:157–164.

Reusch, P., H. Wagdy, R. Reusch, E. Wilson, and H. E. Ives. 1996. Mechanical strain increases smooth muscle and decreases nonmuscle myosin expression in rat vascular smooth muscle cells. *Circ. Res.* 79:1046–1053.

Rotsch, C., and M. Radmacher. 2000. Drug-induced changes of cytoskeletal structure and mechanics in fibroblasts: an atomic force microscopy study. *Biophys. J.* 78:520–535.

Sackin, H. 1995. Stretch-activated ion channels. *Kidney Int.* 48: 1134–1147.

Satcher, R., C. F. Dewey Jr., and J. H. Hartwig. 1997. Mechanical remodeling of the endothelial surface and actin cytoskeleton induced by fluid flow. *Microcirculation.* 4:439–453.

Satcher Jr., R. L., and C. F. Dewey Jr. 1996. Theoretical estimates of mechanical properties of the endothelial cell cytoskeleton. *Biophys. J.* 71:109–118.

So, P. T. C., T. French, W. M. Yu, K. M. Berland, C. Y. Dong, and E. Gratton. 1995. Time-resolved fluorescence microscopy using two-photon excitation. *Bioimaging*. 3:49–63.

So, P. T., K. Konig, K. Berland, C. Y. Dong, T. French, C. Buhler, T. Ragan, and E. Gratton. 1998. New time-resolved techniques in two-photon microscopy. *Cell. Mol. Biol. (Noisy-le-grand)*. 44:771–793.

Songu-Mize, E., X. Liu, J. E. Stones, and L. J. Hymel. 1996. Regulation of Na+,K+-ATPase alpha-subunit expression by mechanical strain in aortic smooth muscle cells. *Hypertension.* 27:827–832.

Stamenovic, D., and M. F. Coughlin. 1999. The role of prestress and architecture of the cytoskeleton and deformability of cytoskeletal filaments in mechanics of adherent cells: a quantitative analysis. *J. Theor. Biol.* 201:63–74.

Stamenovic, D., and M. F. Coughlin. 2000. A quantitative model of cellular elasticity based on tensegrity. *J. Biomech. Eng.* 122:39–43.

Thoumine, O., A. Ott, O. Cardoso, and J. J. Meister. 1999. Microplates: a new tool for manipulation and mechanical perturbation of individual cells. *J. Biochem. Biophys. Methods.* 39:47–62.

Wagner, C. T., W. Durante, N. Christodoulides, J. D. Hellums, and A. I. Schafer. 1997. Hemodynamic forces induce the expression of heme oxygenase in cultured vascular smooth muscle cells. *J. Clin. Invest.* 100:589–596.

Wang, N., J. P. Butler, and D. E. Ingber. 1993. Mechanotransduction across the cell surface and through the cytoskeleton [see comments]. *Science.* 260:1124–1127.

Wang, N., and D. E. Ingber. 1994. Control of cytoskeletal mechanics by extracellular matrix, cell shape, and mechanical tension. *Biophys. J.* 66:2181–2189.

Wilson, E., Q. Mai, K. Sudhir, R. H. Weiss, and H. E. Ives. 1993. Mechanical strain induces growth of vascular smooth muscle cells via autocrine action of PDGF. *J. Cell Biol.* 123:741–747.

Wu, Z., K. Wong, M. Glogauer, R. P. Ellen, and C. A. McCulloch. 1999. Regulation of stretch-activated intracellular calcium transients by actin filaments. *Biochem. Biophys. Res. Commun.* 261:419–425.

Yamada, S., D. Wirtz, and S. C. Kuo. 2000. Mechanics of living cells measured by laser tracking microrheology. *Biophys. J.* 78:1736–1747.